

# Poly-Spline Finite Element Method

TESEO SCHNEIDER, JÉRÉMIE DUMAS, XIFENG GAO, MARIO BOTSCH, DANIELE PANOZZO, and DENIS ZORIN, New York University



Fig. 1. A selection of the automatically generated pure hexahedral and hexahedral-dominant meshes in our test set. The colors denote the type of basis used. In the bottom-right, we show the result of a Poisson problem solved over a hex-dominant, polyhedral mesh.

We introduce an integrated meshing and finite element method pipeline enabling black-box solution of partial differential equations in the volume enclosed by a boundary representation. We construct a hybrid hexahedral-dominant mesh, which contains a small number of star-shaped polyhedra, and build a set of high-order basis on its elements, combining triquadratic B-splines, triquadratic hexahedra (27 degrees of freedom), and harmonic elements. We demonstrate that our approach converges cubically under refinement, while requiring around 50% of the degrees of freedom than a similarly dense hexahedral mesh composed of triquadratic hexahedra. We validate our approach solving Poisson’s equation on a large collection of models, which are automatically processed by our algorithm, only requiring the user to provide boundary conditions on their surface.

## ACM Reference format:

Teseo Schneider, Jérémie Dumas, Xifeng Gao, Mario Botsch, Daniele Panozzo, and Denis Zorin. 2022. Poly-Spline Finite Element Method . 1, 1, Article 1 (June 2022), 12 pages.

DOI: 10.1145/nnnnnnn.nnnnnnn

## 1 INTRODUCTION

The numerical solution of partial differential equations is ubiquitous in computer graphics and engineering applications, ranging from the computation of UV maps and skinning weights, to the simulation of elastic deformations, fluids, and light scattering.

The finite element method (FEM) is the most commonly used discretization of PDEs, especially in the context of structural and thermal analysis, due to its generality and rich selection of off-the-shelf commercial implementations. Ideally, a PDE solver should be a “black box”: the user provides as input the domain boundary,

boundary conditions, and the governing equations, and the code returns an evaluator that can compute the value of the solution at any point of the input domain. This is surprisingly far from being the case for all existing open-source or commercial software, despite the research efforts in this direction and the large academic and industrial interest.

To a large extent, this is due to treating meshing and FEM basis construction as two disjoint problems. The FEM basis construction may make a seemingly innocuous assumption (e.g., on the geometry of elements), that lead to exceedingly difficult requirements for meshing software. For example, commonly used bases for tetrahedra are sensitive to the tetrahedron shape, so tetrahedral mesh generators have to guarantee good element shape everywhere: a difficult task which, for some surfaces, does not have a fully satisfactory solution. Alternatively, if few assumptions are made on mesh generation (e.g., one can use elements that work on arbitrary polyhedral domains), the basis and stiffness matrix constructions can become very expensive.

This state of matters presents a fundamental problem for applications that require fully automatic, robust processing of large collections of meshes of varying sizes, an increasingly common situation as large collections of geometric data become available. Most importantly, this situation arises in the context of machine learning on geometric and physical data, when one can run large numbers of simulations to learn from, as well as problems of shape optimization, which require solving PDEs in the inner optimization loop on a constantly changing domain.

*Overview.* We propose an integrated pipeline, considering meshing and element design as a single challenge: we make the tradeoff

between mesh quality and element complexity/cost *local*, instead of making an a priori decision for the whole pipeline. We generate high quality, simple, and regularly arranged elements for most of the volume of the shape, with more complex and poor quality polyhedral shapes filling the remaining gaps [Sokolov et al. 2016; Gao et al. 2017a]. Our idea is to match each element to a basis construction, with well-shaped elements getting the simplest and most efficient basis functions with complex polyhedral element formulations used only when necessary to handle the transitions between regular regions, which are the ones that are topologically and geometrically more challenging.

The “ideal” FEM construction in 3D are splines on regular cubic lattices. This basis has potential to be *both* accurate and efficient: it has a single degree of freedom per element, except at the boundary, yet, has full approximation power corresponding to the degree of the spline. This observation is one of the foundations of *isogeometric analysis* in 3D [Hughes et al. 2005; Cottrell et al. 2009], and it has been shown to outperform traditional FEM bases. Unfortunately, it is easy to define and implement only for fully regular grids, which is not practical for most input geometries. The next best thing are spline bases on *pure hexahedral* meshes: while smooth constructions for polar configurations exist [Toshniwal et al. 2017], a solution applicable to general hexahedral meshes whose interior singular curves meet is still elusive, restricting this construction to simple shapes. Padded hexahedral-meshes [Maréchal 2009a] are necessary to ensure a good boundary approximation for both regular and polycube hexahedral meshing methods, but they unfortunately cannot be used by these constructions since their interior curve singularities meet in the padding layer.

We propose a hybrid construction that sidesteps these limitations: we use ideal spline elements only on fully regular regions, and fill the elements that are touching singular edges, or that are not hexahedra, with local constructions (harmonic elements for polyhedra, triquadratic polynomial elements for hexahedra). This construction further relaxes requirements for meshing, since it works on general hexahedral meshes (without any restriction on their singularity structure) but also directly supports *hex-dominant* meshes, which can be robustly generated with modern field-aligned methods [Gao et al. 2017a; Sokolov et al. 2016]. These meshes consist mostly of well-shaped hexahedra with locally regular mesh structure, but also contain other general polyhedra. Our construction takes advantage of this high regularity, adding a negligible overhead over the ideal FEM basis only for the sparse set of non-regular elements.

We demonstrate that our proposed *Poly-Spline* FEM retains, to a large extent, both the approximation and performance benefits of splines, at the cost of the increasing basis construction complexity, and at the same time, works for a class of meshes that can be robustly generated for most shapes with existing meshing algorithms

We show on a large data set that our method is capable of operating in the “black-box” manner described above, opening doors to a range of new applications.

## 2 RELATED WORK

When numerically solving PDEs using the finite element method, one has to discretize the spatial domain into finite elements and define shape functions on these elements. Since shape functions,

element types, and mesh generation are closely related, we discuss the relevant approaches in tandem.

For complex spatial domains, the discretization is frequently based on the Delaunay triangulation [Shewchuk 1996] or Delaunay tetrahedrization [Si 2015], respectively, since those tessellations can be computed in a robust and automatic manner. Due to their simplicity and efficiency, linear shape functions are often the default choice for graphics applications the resulting triangular or tetrahedral elements [Hughes 2000], although they are known to suffer from locking for stiff PDEs, such as nearly incompressible elastic materials [Hughes 2000].

This locking problem can be avoided by using bilinear quadrangular or trilinear hexahedral elements ( $Q_1$  elements), which have the additional advantage of yielding a higher accuracy for a given number of elements [Cifuentes and Kalbag 1992; Benzley et al. 1995]. Triquadratic hexahedral elements ( $Q_2$ ) provide even higher accuracy and faster convergence under mesh refinement (cubic in  $L^2$  for  $Q_2$  vs. quadratic for  $Q_1$ ), but their larger number of degrees of freedom lead to high memory consumption and computational cost.

The main idea of isogeometric analysis (IGA) [Hughes et al. 2005; Cottrell et al. 2009] is to employ the same spline basis for defining the CAD geometry as well as for performing numerical analysis. Using quadratic splines on hexahedral elements results in the same cubic convergence order as  $Q_2$  elements, but at the much lower cost of *one* degree of freedom per element (comparable to  $Q_1$  elements). This efficiency, however, comes at the price of a very complex implementation for non-regular hexahedral meshes. Moreover, generating IGA-compatible meshes from a given general boundary surface is still an open problem [Aigner et al. 2009; Martin and Cohen 2010; Li et al. 2013b].

A standard method for volumetric mesh generation is through hierarchical subdivision of an initial regular hexahedral mesh, leading to so-called octree meshes [Maréchal 2009b; Ito et al. 2009; Zhang et al. 2013]. The T-junctions resulting from adaptive subdivision can be handled by using T-splines [Sederberg et al. 2004; da Veiga et al. 2011] as shape functions. While this meshing approach is very robust, it has problems representing geometric features that are not aligned with the principal axes.

Even when giving up splines or T-splines for standard  $Q_1/Q_2$  elements, the automatic generation of the required hexahedral meshes is problematic. Despite the progress made in this field over the last decade, *automatically* generating pure hexahedral meshes that (i) have sufficient element quality, (ii) are not too dense, and (iii) align to geometric features is still unsolved. Early methods based on paving or sweeping [Owen and Saigal 2000; Yamakawa and Shimada 2003; Staten et al. 2005; Shepherd and Johnson 2008] require complicated handling of special cases and generate too many singularities. Polycube methods [Gregson et al. 2011; Li et al. 2013a; Livesu et al. 2013; Huang et al. 2014; Fang et al. 2016; Fu et al. 2016] and field-aligned methods [Nieser et al. 2011; Huang et al. 2011; Li et al. 2012; Jiang et al. 2014] are interesting research venues, but they are currently not robust and often fail to produce a valid mesh.

However, if the strict requirement of producing hexahedral elements only is relaxed, field-aligned methods [Sokolov et al. 2016; Gao et al. 2017a] can robustly and automatically create hex-dominant

polyhedral meshes. The idea is to build local volumetric parameterizations aligned with a specified directional field, and constructing the mesh from traced isolines of that parameterization, inserting general polyhedra if necessary. Their drawback is that they produce *hex-dominant* meshes, which are not directly supported by most FEM codes.

One option is to split these polyhedra into standard elements, leading to a mixed FEM formulation. For instance, the field-aligned meshing of Sokolov et al. [2016] extract meshes that are composed of hexahedra, tetrahedra, prisms, and pyramids. However, the quality of those split elements is hard to control in general. An interesting alternative is to avoid the splitting of polyhedra and instead incorporate them into the simulation, for instance through mimetic finite differences [Lipnikov et al. 2014], the virtual element method [Beirão Da Veiga et al. 2013], or polyhedral finite elements [Manzini et al. 2014]. The latter employ generalized barycentric coordinates as shape functions, such as mean value coordinates [Floater et al. 2005; Ju et al. 2005], harmonic coordinates [Joshi et al. 2007], or minimum entropy coordinates [Hormann and Sukumar 2008]. From those options, harmonic coordinates seem most suitable since they generalize both linear tetrahedra and trilinear hexahedra to general non-convex polyhedra [Martin et al. 2008; Bishop 2014]. While avoiding splitting or remeshing hex-dominant meshes, the major drawback of polyhedral elements is the high cost for computing and integrating their shape functions.

In the above methods the meshing stage either severely restricts admissible shape functions, or the element type puts (too) strong requirements on the meshing. In contrast, we use the most efficient elements where possible and the most flexible elements where required, which enables the use of robust and automatic hex-dominant mesh generation.

### 3 ALGORITHM OVERVIEW

In this section, we introduce the main definitions we use in our algorithm description, and outline the structure of the algorithm.

*Input complex and subcomplexes.* The input to our algorithm is a 3D polyhedral complex  $\mathcal{M}$ , with vertices  $\mathbf{v}_i \in \mathbb{R}^3$ ,  $i = 1 \dots V$ , consisting of polyhedral cells  $C_i$ ,  $i = 1 \dots N_c$ , most of which are hexahedra. Figure 2 shows a two-dimensional example of such complex. The edges, faces and cells of the mesh are defined combinatorially, that is, edges are pairs of vertices, faces are sequences of edges, and cells are surface meshes formed by faces. We assume that 3D positions of vertices are also provided as input and that  $\mathcal{M}$  is three-manifold, i.e., that there is a way to identify vertices, edges, faces and cells with points, curves, surface patches and simple volumes, such that their union is a three-manifold subset of  $\mathbb{R}^3$ .

We assume that for any hexahedron there is at most one non-hexahedral cell sharing one of its faces or edges, which can be achieved by refinement. We also assume that no two polyhedral cells are adjacent, and that no polyhedron touches the boundary; which can also be achieved by merging polyhedral cells and/or refinement. This preprocessing step is discussed in Section 6. As a consequence of our refinement, *all faces of  $\mathcal{M}$  are quadrilateral*.

One of the difficulties of using general polyhedral meshes for basis constructions is that, unlike the case of, for example, pure

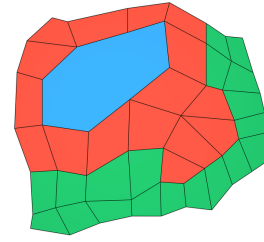


Fig. 2. Complexes involved in our construction. In green we show  $\mathcal{S}$ , in red  $\mathcal{Q}$ , and in blue  $\mathcal{P}$ .

tetrahedral meshes, there is no natural way to realize all elements of the mesh in 3D just from vertex positions (e.g., for a tetrahedral mesh, linear interpolation for faces and cells is natural). This requires constructing bases on an explicitly defined parametric domain associated with the input complex.

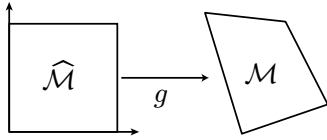
For this purpose, we define a certain number of complexes related to the original complex  $\mathcal{M}$  (Figure 2). There are two goals for introducing these: defining the parametric domain for the basis, and defining the *geometric map*, which specifies how the complex is realized in three-dimensional *physical space*.

- $\mathcal{H} \subseteq \mathcal{M}$  is the hexahedral part of  $\mathcal{M}$ , consisting of hexahedra  $H$ .
- $\mathcal{P} = \mathcal{M} \setminus \mathcal{H}$  is the non-hexahedral part of  $\mathcal{M}$ , consisting of polyhedra  $P$ .
- $\mathcal{S} \subseteq \mathcal{H}$  is the complex consisting of spline-compatible hexahedra  $S$  defined in Section 4.1.
- $\mathcal{Q} = \mathcal{H} \setminus \mathcal{S}$  is the spline-incompatible pure-hexahedral part of  $\mathcal{M}$ .

Note that the sub-complexes of  $\mathcal{M}$  are nested:  $\mathcal{S} \subseteq \mathcal{H} \subseteq \mathcal{M}$ .

In the context of finite elements, the distinction between *parametric space* and *physical space* is critical: the bases on the hexahedral part of the mesh are defined in terms of parametric space coordinates, where all hexahedra are unit cubes; this makes it possible to define simple, accurate and efficient bases. However, the derivatives in the PDE are taken with respect to physical space variables, and the unknown functions are naturally defined on the physical space. Remapping these functions to the parametric space is necessary to discretize the PDE using our basis. We define parametric domains  $\widehat{\mathcal{M}}$ ,  $\widehat{\mathcal{H}}$ ,  $\widehat{\mathcal{S}}$ , and  $\widehat{\mathcal{Q}}$  corresponding to  $\mathcal{M}$ ,  $\mathcal{H}$ ,  $\mathcal{S}$ , and  $\mathcal{Q}$ , respectively.  $\widehat{\mathcal{H}}$  consists of unit cubes  $\widehat{H}$ , one per hexahedron  $H$  with corresponding faces identified, and  $\widehat{\mathcal{S}}$  and  $\widehat{\mathcal{Q}}$  are its subcomplexes. The complete parametric space  $\widehat{\mathcal{M}}$  is obtained by adding a set of polyhedra for  $\mathcal{P}$ , defined using the geometric map as described below. For polyhedra, physical and parametric space coincide.

*Geometric map and complex embedding.* The input complex, as it is typical for mesh representations, does not define a complete geometric realization of the complex: rather it only includes vertex positions and element connectivity. We define a complete geometric realization as the *geometric map*  $g: \widehat{\mathcal{M}} \rightarrow \mathbb{R}^3$ , from the parametric domain  $\widehat{\mathcal{M}}$  to the physical space. We use  $\widehat{\mathbf{x}}$  for points in the parametric domain, and  $\mathbf{x}$  for points in the physical space, and denote the image of the geometric map  $\Omega = g(\widehat{\mathcal{M}})$  (Figure 3).

Fig. 3. Illustration of the geometric mapping for  $\mathcal{H}$ .

The definition requires bootstrapping:  $g$  is first defined on  $\widehat{\mathcal{H}}$ . For example, the simplest geometry map  $g$  on  $\widehat{\mathcal{M}}$  can be obtained by trilinear interpolation:  $g$  restricted to a unit cube  $\widehat{H} \subset \widehat{\mathcal{M}}$  is a trilinear interpolation of the positions of the vertices of its associated hexahedron  $H$ . We make the following assumption about  $g(\widehat{\mathcal{H}})$ : the map is bijective on the faces of  $\mathcal{H}$ , corresponding to the boundary of any polyhedral cell  $P$ , and the union of the images of these faces does not self-intersect and encloses a volume  $P'$ . Section 6 explains how this is ensured. Then we complete  $\widehat{\mathcal{M}}$  by adding the volume  $P'$  as the parametric domain for  $P$ . We add this volume to the parametric domain  $\widehat{\mathcal{M}}$ , identifying corresponding faces with faces in  $\widehat{\mathcal{H}}$ , and defining the geometric map to be identity on these domains.

The simplest trilinear map is adequate for elements of the mesh outside the regular part  $\mathcal{S}$ , but is insufficient for accuracy on the regular part, as discussed below. We consider a more complex definition of  $g$  ensuring  $C^1$  smoothness across interior edges and faces of  $\mathcal{S}$ , described in Section 5, after we describe our basis construction. Our construction is *isoparametric*, that is, it uses the same basis for the geometry map as for the solution.

*Overview of the basis and discretization construction.* Given an input complex  $\mathcal{M}$ , we construct a set of bases  $\widehat{\phi}_i: \widehat{\mathcal{M}} \rightarrow \mathbb{R}, i = 1 \dots N$  such that:

- the restriction of basis function  $\widehat{\phi}_i$  to spline compatible hexahedral domains  $\widehat{S} \in \widehat{\mathcal{S}}$  is a spline basis function;
- the restriction to hexahedra  $\widehat{Q} \in \widehat{\mathcal{Q}}$  is a standard triquadratic ( $Q_2$ ) element function;
- the restriction to polyhedra  $\widehat{P} \in \widehat{\mathcal{P}}$  is a harmonic-based nonconformal, third-order accurate basis function.

The degrees of freedom (dofs) corresponding to basis functions  $\widehat{\phi}_i$  are associated with:

- each hexahedron either in  $\mathcal{S}$  or adjacent to a spline-compatible one (*spline cell dofs*);
- each boundary vertex, edge, or face of  $\mathcal{S}$  (*spline boundary dofs*); these are needed to have correct approximation on the boundary;
- each vertex, edge, face, and cell of  $\mathcal{Q}$  (*triquadratic element degrees of freedom*).

The total number of degrees of freedom is denoted by  $N$ . While most of the construction is independent of the choice of PDE (we assume it to be second-order), with a notable exception of the consistency condition for polyhedral elements, we use Poisson equation to be more specific.

Note that hexahedra adjacent to  $\mathcal{S}$ , but not in  $\mathcal{S}$  (i.e., hexahedra in  $\mathcal{Q}$ ) get both spline dofs and triquadratic element dofs: such a cell may have  $\geq 28$  dofs instead of 27.

Polyhedral cells are not assigned separate degrees of freedom: the basis functions with support overlapping polyhedra are those associated with dofs at incident hexahedra.

We assemble the standard stiffness matrix for an elliptic PDE, element-by-element, performing integration on the hexahedra  $\widehat{H}$  of  $\widehat{\mathcal{M}}$  and polyhedra  $P$ . The entry  $K_{ij}$  of the stiffness matrix for the Poisson's equation is computed as follows:

$$K_{ij} = - \sum_{\widehat{C} \in \widehat{\mathcal{M}}} \int_{g(\widehat{C})} \nabla_{\mathbf{x}} \phi_i(\mathbf{x}) \cdot \nabla_{\mathbf{x}} \phi_j(\mathbf{x}) \, d\mathbf{x}, \quad (1)$$

where  $\phi_i = \widehat{\phi}_i \circ g^{-1}$ . The actual integration is performed on the elements in the parametric domain  $\widehat{\mathcal{M}}$ , using a change of variables  $\mathbf{x} = g(\widehat{\mathbf{x}})$  for every element:

$$K_{ij} = - \sum_{\widehat{C} \in \widehat{\mathcal{M}}} \int_{\widehat{C}} \nabla_{\widehat{\mathbf{x}}} \widehat{\phi}_i(\widehat{\mathbf{x}})^T \mathbf{A} \nabla_{\widehat{\mathbf{x}}} \widehat{\phi}_j(\widehat{\mathbf{x}}) |Dg| \, d\widehat{\mathbf{x}} \quad (2)$$

where  $\mathbf{A}(\widehat{\mathbf{x}})$  is the metric tensor of the geometric map  $g$  at  $\widehat{\mathbf{x}}$ , given by  $Dg^T Dg$ .

In the next sections, we describe the construction of the basis on each element type, the geometric map, and stiffness matrix construction.

#### 4 BASIS CONSTRUCTION

We seek to construct a basis on  $\Omega$  which has the following properties:

- (1) it is  $C^0$  everywhere on  $\Omega$ ,  $C^1$  at regular edges and vertices, and  $C^\infty$  within each  $H$  and  $P$  (polynomials on hexahedra).
- (2) it has approximation order 3 on each  $H$  and  $P$ .

The unknown function  $u$  on the domain  $\Omega$  is approximated by  $u_h = \sum_i u_i \phi_i$ , where  $\phi_i$  are the basis functions. The support of each basis function is a union of a set of the images under  $g$  of cells in  $\widehat{\mathcal{M}}$ .

The actual representation of the basis, that allows us to perform per-element construction of the stiffness matrix, consists of three parts.

The first two parts are local: we define a *local* set of dofs, and a *local* basis. For hexahedral elements, there are several types of local polynomial bases each coming with its set of local dofs, associated with a *local control mesh* for the element. These basis functions are encoded as sets of polynomial coefficients. For polyhedral elements, all local basis functions are weighted combinations of harmonic kernel functions and a triquadratic polynomial, so these are encoded as kernel centers, weights and polynomial coefficients.

The third part is the *local-to-global* linear map that represents local dofs in terms of the global ones. Importantly, unlike most standard FEM formulations, our local-to-global maps are not necessarily simply identifying local dofs with one of the global ones: some local dofs are linear combinations of global ones. These maps are formally represented by  $m \times N$  matrices, where  $m$  is a small number of local dofs, and  $N$  is the total number of global dofs. However, as the elements local dofs depend only on nearby global dofs, these matrices have a small number of nonzeros, and can be encoded in a compact form.

Next, we consider the construction of these three elements (set of local basis functions, set of local dofs, local-to-global map) for

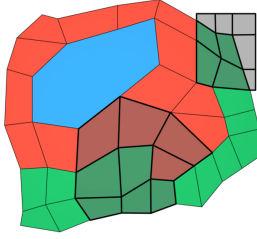


Fig. 4. Spline local grid (shown in dark), for an internal and boundary quadrilateral. The color codes are as defined in Figure 2

each of our three element types. But before we can construct the basis for each element, hexahedral elements need to be classified into  $\mathcal{S}$  (spline-compatible) and  $\mathcal{Q}$ .

#### 4.1 Spline-compatible hexahedral elements

We define a hexahedron  $H$  to be spline-compatible, if its one-ring cell neighborhood is a  $3 \times 3 \times 3$  regular grid, possibly cut on one or more sides if  $H$  is on the boundary, see Figure 4.

The *local dofs* of this element type form a  $3 \times 3 \times 3$  grid (for interior elements), with the element in the center (Figure 5 left); for boundary elements, there are still 27 dofs, ensuring a full triquadratic polynomial reproduction. As a single layer with 9 dofs is missing, we add an extra degree of freedom for each face of the local  $3 \times 3 \times 2$  grid corresponding to the boundary. Other cases are handed in a similar manner; e.g. the configuration for a regular corner is shown in Figure 5, right.

The *basis functions* in this case are just the standard triquadratic uniform spline basis functions for interior hexahedra. For the boundary case, we use the knot vector  $[0, 0, 0, 1, 2, 3]$  in the direction perpendicular to the boundary. Finally, the *local-to-global* map simply identifies local basis dofs with corresponding global ones.

Compared to a standard  $Q_2$  FEM element, the ratio of degrees of freedom to the number of elements is much lower (a single degree of freedom per element for splines), although the approximation order is the same.

#### 4.2 $Q_2$ hexahedral elements

This element is used for all remaining hexahedra. This is a standard element, widely used in finite element codes. *Local dofs* for this element are associated with the element vertices, edge midpoints, face centers, and cell centers.

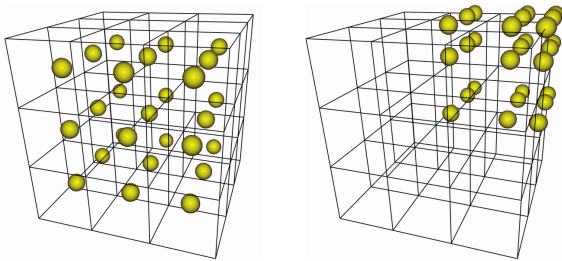


Fig. 5. Spline hex degrees of freedom.

The *local basis functions* for the element are obtained as the tensor product of the interpolating quadratic bases on an interval  $[0, 1]$ , consisting of  $(t - \frac{1}{2})(t - 1)$ ,  $(t - \frac{1}{2})t$  and  $(t - 1)t$ .

The only complicated part in the case of  $Q_2$  elements is the definition of the local-to-global map. For the two-dimensional setting, it is illustrated in Figure 6.

The difficulty in the construction of this map is due to the interface between spline elements and  $Q_2$  elements, and the need to ensure continuity between the two. In the two-dimensional case, suppose that a  $Q_2$  element shares an edge with exactly one quad spline element  $S$ . Let  $u_{ij}$ ,  $i, j = 1 \dots 3$ , be the global dofs of the spline element, and let  $q_{ij}$ ,  $i, j = 1 \dots 3$ , be the degrees of freedom of the  $Q_2$  element, as shown in the picture.

In this case, we ensure  $C^0$  continuity of the basis by expressing the values of the polynomials on  $Q \in \mathcal{Q}$  at the shared boundary points in terms of global degrees of freedom.

Since both the  $Q_2$  and the spline basis restricted to an edge are quadratic polynomials, they only need to be equal on three distinct points of the edge to ensure continuity. By noticing that the  $Q_2$  basis is interpolatory at the nodes, it is enough to evaluate the spline basis at these edge nodes.

For the two-dimensional example in Figure 6, the local-to-global map for the local dofs  $q_{31}$ ,  $q_{32}$  and  $q_{33}$  along the edge (in blue) that the  $Q_2$  element shares with the spline is obtained as follow:

$$\begin{aligned} q_{31} &= \frac{1}{4}(u_{11} + u_{12} + u_{21} + u_{22}) \\ q_{32} &= \frac{3}{8}(u_{12} + u_{22}) + \frac{1}{16}(u_{11} + u_{21} + u_{13} + u_{23}) \\ q_{33} &= \frac{1}{4}(u_{12} + u_{13} + u_{22} + u_{23}) \end{aligned} \quad (3)$$

In 3D, the construction is similar. We first identify all spline bases overlapping with a local dof  $q_{ij}$  on the boundary of a  $Q_2$  element (i.e., a vertex, edge, or face dof). To determine the weights of the local-to-global map, we evaluate each spline basis on the local dof  $q_{ij}$  and set it as weight.

The remaining degrees of freedom of the  $Q_2$  element are identified with global  $Q_2$  degrees of freedom at the same locations. We note once again, that at the center of cells in  $\mathcal{Q}$  with neighboring cells in  $\mathcal{S}$ , there are *two* dofs, one spline, and one  $Q_2$ .

#### 4.3 Basis construction on polyhedral cells

The construction of the basis on the polyhedral cells is quite different from the construction of the basis on hexahedra. For hexahedra,

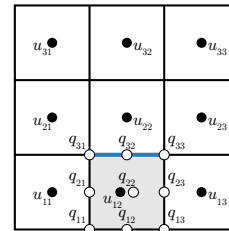


Fig. 6.  $Q_2$  local to global map for an element adjacent to a single spline element.

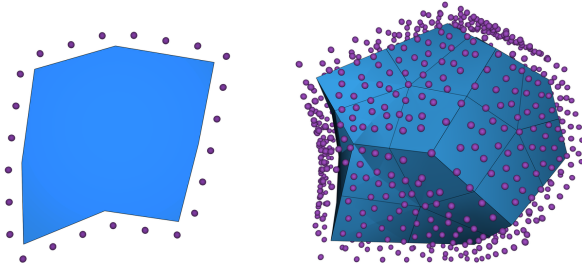


Fig. 7. Local basis for a polygon consists of the set of triquadratic polynomials and harmonic kernels centered at shown locations.

the basis functions are defined on the parametric domain  $\widehat{\mathcal{M}}$ , and are remapped to  $\Omega \subset \mathbb{R}^3$  via the geometric map. For polyhedra, we construct the basis directly in physical space.

We follow the general approach of [Martin et al. 2008] with two important alterations designed to ensure third-order convergence.

Recall that we assume that all polyhedron faces are quadrilateral, and all polyhedra are surrounded by hexahedra (specifically,  $Q_2$  hexahedra, as their neighborhood is not regular). We use the degrees of freedom on the faces of these elements as degrees of freedom for the polyhedra, therefore the *local-to-global* map in this case is trivial.

Each dof is already associated with a basis function  $\phi_j(\mathbf{x})$  defined on the hexahedra adjacent to the polyhedron. We construct the extension of  $\phi_j$  to the polyhedron  $P$ , from  $k$  harmonic kernels  $\psi_i$  centered at points  $\mathbf{z}_i$  outside the polyhedron, and triquadratic monomials  $q_d(\mathbf{x})$ ,  $d = 1 \dots 10$ , as

$$\phi_j|_P(\mathbf{x}) = \sum_{i=1}^k w_i^j \psi_i(\mathbf{x}) + \sum_{d=1}^{10} a_d^j q_d(\mathbf{x}) = (\mathbf{w}^j)^T \boldsymbol{\psi}(\mathbf{x}) + (\mathbf{a}^j)^T \mathbf{q}(\mathbf{x}), \quad (4)$$

where  $\psi_i(\mathbf{x}) = \|\mathbf{x} - \mathbf{z}_i\|^{-1}$ .

The weights  $w_i^j$  and  $a_d^j$ , following [Martin et al. 2008], are determined using a least squares fit to match the values of the basis  $\phi_j$  evaluated on a set of points sampled on the boundary of the polyhedron.

In [Martin 2011], it is shown that this construction automatically guarantees linear polynomial reproduction, if  $q_d$  are linear; the quadratic case is fully analogous. However, this condition is insufficient for high-order convergence, because our basis is *non-conforming*. In the context of the second-order PDEs we are considering, it means that it lacks  $C^0$  continuity on the boundary of the polyhedron. For this type of elements, additional *consistency* conditions are required to ensure high-order convergence. These conditions depend on the PDE that we need to solve.

*FEM theory detour.* To achieve higher order convergence *three* conditions need to be satisfied: (1) polynomial reproduction; (2) consistency, which we discuss in more detail below and (3) quadrature accuracy. We refer to standard FEM texts such as [Braess 2007] for details, as well as to virtual element method literature (e.g., [de Dios et al. 2016] is closely related).

Rigorous convergence theory would also need to include stability analysis, which often presents the main technical hurdle and is

beyond the scope of this paper. We present numerical evidence that our method has the expected behavior.

To satisfy the third condition, we use high-order quadrature on the polyhedron: we decompose it into tetrahedra and use Gaussian quadrature points in each tetrahedra (the decomposition is detailed in Section 6.1). Polynomial reproduction is ensured by construction of the basis above.

The second constraint, consistency, requires further elaboration. The standard way to find the solution of a PDE for a finite element system is to consider its weak form: find  $u$  such that

$$\int_{\Omega} \Delta u v = - \int_{\Omega} \nabla u \cdot \nabla v = f, \quad \forall v \quad (5)$$

for the Poisson's equation. *Remark.* We omit, for readability, the integration variable  $d\mathbf{x}$ : in the remaining formulas we use integration over the physical space exclusively, in practice carried over in the parametric space by adding the Jacobian of the geometric map.

Then,  $u$  is approximated by  $u_h = \sum_i u_i \phi_i$ , and  $v$  is taken to be in the space spanned by the bases  $\phi_j$ . The stiffness matrix entries are obtained as  $K_{ij} = \sum_C \int_C \nabla \phi_i \cdot \nabla \phi_j$ , where the integral is computed per element  $C$ , leading to the discrete system  $\mathbf{K}\mathbf{u} = \mathbf{f}$ .

For non-conforming elements, in general, we cannot rely on this standard approach in formulating the system: for example, if we consider piecewise-constant elements for the Poisson's equation, the stiffness matrix will be all zeros.

However, for a given PDE, one can construct converging non-conforming elements. One condition that is typically used, is to require that the discrete matrix, constructed per element as above, gives us *exact* values of the weak-form integral for all polynomials reproduced by the basis (cf.  $k$ -consistency property in [de Dios et al. 2016]).

As our basis reproduces triquadratic monomials (i.e. they are in the span of bases  $\phi_i$ ), we have  $q_d(\mathbf{x}) = \sum_i q_d^i \phi_i(\mathbf{x})$ . To ensure consistency, we require that any *nonconforming basis functions*  $\phi_j$  satisfies

$$\int_{g(\widehat{\mathcal{M}})} \Delta q_d \phi_j = \sum_i K_{ij} q_d^i \quad (6)$$

for all triquadratic monomials  $q_d$ .

To convert this equation to an equation for the unknown coefficients  $w_i^j$  and  $a_m^j$ , we observe that

$$\sum_i K_{ij} q_d^i = - \int_{g(\widehat{\mathcal{M}})} \left( \sum_i q_d^i \nabla \phi_i \right) \nabla \phi_j = \int_{g(\widehat{\mathcal{M}})} \nabla q_d \nabla \phi_j \quad (7)$$

due to the polynomial reproduction property. Separating the integral into the part over the hexahedra and over the polyhedron, we write

$$\begin{aligned} \sum_i K_{ij} q_d^i &= C_H - \int_P \nabla q_d \nabla \left( (\mathbf{w}^j)^T \boldsymbol{\psi} + (\mathbf{a}^j)^T \mathbf{q} \right) \\ &= C_H + \mathbf{b}^T (\mathbf{w}^j) + \mathbf{c}^T (\mathbf{a}^j) \end{aligned} \quad (8)$$

where

$$C_H = \sum_{\widehat{C} \in \widehat{\mathcal{M}} \setminus P} \int_{g(\widehat{C})} \nabla q_d \nabla \phi_j, \quad \mathbf{b} = - \int_P \nabla q_d \nabla \boldsymbol{\psi}, \quad \text{and} \quad \mathbf{c} = - \int_P \nabla q_d \nabla \mathbf{q}.$$

Similarly, the left-hand side of Equation (6) is reduced to a linear combination of  $w_j$  and  $a^j$ . This forms a set of additional constraints, for the coefficients of the basis functions on the polyhedron. To

enforce them on each polyhedron, we solve a constrained least square system for each nonconforming basis function and store the obtained coefficients. Importantly, the addition of constraints to the least squares system does not violate the polynomial reproduction property on the polyhedron. This can be seen as follows.

Let  $\ell$  be the linear combination of basis functions  $\phi_i$  overlapping  $P$  that yields a triquadratic monomial  $q_d$  when restricted to  $P$ . Then  $\ell$  is continuous on  $\Omega$ : the samples at the points of the boundary are quadratic, therefore, match exactly the quadratic continuation to adjacent hexahedra.

The consistency condition (Equation 6) applied to  $\ell$  simply states that it satisfies the integration by parts formula, which it does as it is  $C^0$  at the element boundaries, and smooth on the elements:

$$\sum_C \int_C \Delta q_d \ell = - \sum_C \int_C \nabla q_d \nabla \ell.$$

We conclude that  $\ell$  is in the space defined by the consistency constraint, and imposing this constraint preserves polynomial reproduction.

#### 4.4 Imposing boundary conditions

We consider two standard types of boundary conditions: Dirichlet (fixed function values on the boundary) and Neumann (fixed normal derivatives at the boundary). Neumann (also known as natural) boundary conditions, are handled in the context of the variational formulation of the problem as extra integral terms, in the case of inhomogeneous conditions. Homogeneous conditions do not require any special treatment, and are imposed automatically in weak formulation.

We assume that the Dirichlet conditions are given as a continuous function defined on the boundary of the domain. For all boundary dofs, we sample the boundary condition on the faces of the domain and perform a least-squares fit to retrieve the nodal values.

### 5 GEOMETRIC MAP CONSTRUCTION

The geometry map is a map from  $\widehat{\mathcal{M}}$  to  $\Omega \subset \mathbb{R}^3$ , defined per element. Its primary purpose is to allow us to construct basis functions  $\widehat{\phi}_i$  on reference domains (i.e., the elements of  $\widehat{\mathcal{M}}$  – unit cubes), and then to remap them to the physical space as  $\phi_i = \widehat{\phi}_i \circ g^{-1}$ . As the local basis on the polyhedral elements is constructed directly in the physical space,  $g$  is the identity on these elements.

The requirements for geometric map are distinct for the spline and  $Q_2$  elements, and are matched by using spline basis itself for  $S$  and  $Q_1$  elements for  $Q_2$  elements.

Because of the geometric mapping  $g$ , for the quadratic spline, the basis  $\phi_i$  does not reproduce polynomials in the physical space; nevertheless, the approximation properties of the basis are retained [Bazilevs et al. 2006].

For  $Q_2$  elements, Arnold et al. [2002] shows that *bilinear* maps are sufficient, and in fact allow to retain reproduction of triquadratic polynomials in the physical space. This is very important for the basis construction on polyhedral elements, as polynomial reproduction on these elements depends on reproduction of polynomials on the polyhedron boundary.

*Computing the geometry map.* If we assume that the input only has vertex positions for  $\mathcal{M}$ , we solve the equations  $g(\widehat{\mathbf{x}}_i) = \mathbf{v}_i$ , which is a linear system of equations in terms of coefficients of  $g$  in the basis we choose. In the trilinear basis, the system is trivial, as the coefficients coincide with the values at  $\mathbf{x}_i$ , and these are simply set to  $\mathbf{v}_i$ . For the triquadratic basis, this is not the case, and a linear system needs to be solved. As in this case the number of degrees of freedom exceeds the number of equations, an additional functional (e.g., Dirichlet energy) can be minimized to obtain a unique solution.

### 6 MESH PREPROCESSING AND REFINEMENT

Without loss of generality, we restrict the meshing discussion to 2D, as the algorithm introduced in this section extends naturally to 3D.

For the sake of simplicity, in this discussion the term polygon refers to non-quadrilateral elements. As previously mentioned, our method can be applied to hybrid meshes without two adjacent polygons and without polygons touching the boundary. While our construction could be extended to support these configurations, we favored introducing one step of refinement to guarantee this condition as a preprocessing. Refining polygonal meshes is an interesting problem on its own: while there is a canonical way to refine quads, there are multiple ways to refine a polygon. We propose the use of polar refinement (Section 6.2), which has the added benefit of allowing us to resample large polygons to obtain a uniform element size. However, to avoid self-intersections between edges during the refinement, we impose each polygon be star-shaped. This condition is often, but not always, satisfied by existing hybrid meshers: we thus introduce a simple merging and splitting procedure to convert hybrid meshes into star-shaped polyhedral meshes (Section 6.1), and then detail our refinement strategy (Section 6.2).

Another advantage of restricting ourselves to star-shaped polygons is that partitioning it into triangles (respectively tetrahedra in 3D) is trivial. This step is required to generate quadrature points for the numerical integration (Section 4.3). Note that for the quadrature the quality of the partitioning is not relevant.

#### 6.1 Mesh preprocessing

We propose a simple and effective algorithm to convert polygonal meshes into star-shaped polygonal meshes, by combining existing polygons until they are star-shaped.

For every non-star-shaped polygon, we pick its barycenter and connect it to all its vertices (Figure 8). This procedure generates a set of intersecting segments, which we use to grow the polygon by merging it with the faces incident to each intersecting segment. The procedure is repeated until no intersections are found, which usually happens in one or two iterations in our experiments. If, during the growing procedure, we reach a boundary, we opt for convex decomposition instead, since it might be impossible to obtain a star-shaped polyhedron by merging if the boundary is concave.

#### 6.2 Polar refinement

Each star-shaped polygon is refined by finding a point in its kernel (Figure 9, a), connecting it to all its vertices (b), splitting each edge with mid-point subdivision and connecting them to the point in the kernel (c), and finally adding rings of quadrilaterals around the

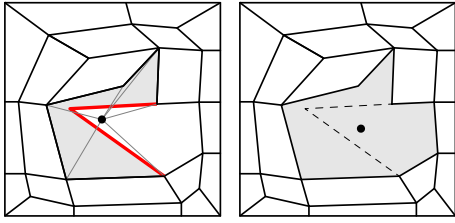


Fig. 8. Our algorithm iteratively merges polygons, until the barycenter of the merged polygon is inside its kernel.

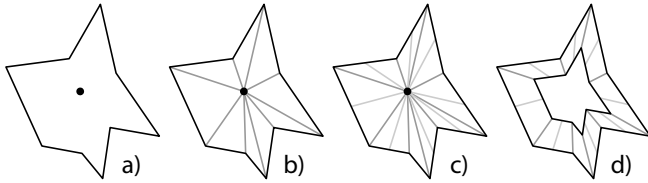


Fig. 9. Polar refinement for polygons.

boundary (d). Figure 10 shows an example of polar refinement in two and three dimensions. The more splits are performed in the edge, the more elements are added. This is a useful feature to homogenize the element size in case the polygons were expanded too much during the mesh preprocessing stage. In our implementation, we split the edges evenly, ensuring that the shortest segment has a length as close as possible to the average edge length of the input mesh.

## 7 EVALUATION

We demonstrate the robustness of our method by solving the Poisson equation on a dataset of pure hex and hybrid meshes, consisting of 206 star-shaped polygonal meshes in 2D, 176 pure hexahedral meshes in 3D, and 29 star-shaped polyhedral meshes in 3D. All those meshes were automatically generated using [Gao et al. 2017a,b]. We show a selection of meshes from our dataset in Figures 1, 11, 12, and 13.

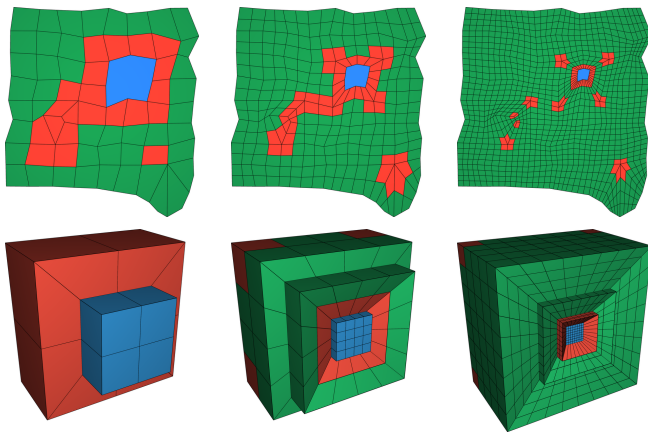


Fig. 10. Example of polar refinement for a polygon and a polyhedron. The bottom view is a cut-through of the actual 3D mesh.

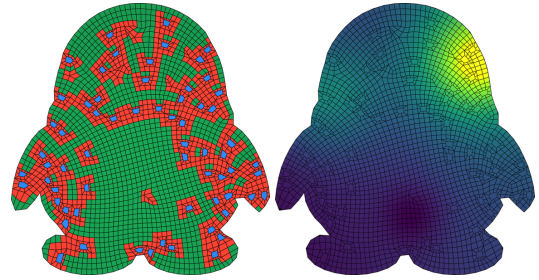


Fig. 11. Solution of the Poisson problem on a 2D polygon.

We evaluated the performance, memory consumption, and running time of our proposed spline construction compared with standard  $Q_1$  and  $Q_2$  elements. For our experiments, we compute the approximation error on a standard Franke’s test function [Franke 1979] in 2D and 3D (Appendix A). Note that in all these experiments, we enforced the consistency constraints on the bases spanning the polyhedral elements, to ensure reproduction of triquadratic polynomials over the polyhedron.

The 2D experiments were run on a PC with an Intel® Core™ i7-5930K CPU @ 3.50GHz with 64 GB, while the 3D dataset was run on a HPC cluster with a memory limit of 64 GB.

*Absolute Errors.* Figure 14 shows a scatter plot of the  $L_2$  and  $L_\infty$  errors on both 2D and 3D datasets, with respect to the number of bases created by each type of elements ( $Q_1$ ,  $Q_2$ , Splines), after one step of polar refinement. The plot shows that in 2D, both the  $L_2$  and  $L_\infty$  errors are about  $\sim 1.5$  order of magnitude lower for our splines compared to  $Q_1$ , while keeping a similar number of dofs. In comparison,  $Q_2$  has lower error, but requires a much larger number of dofs. In 3D the spread of both errors is much larger, and the gain in  $L_\infty$  is less visible, but still present, compared to  $Q_1$ .

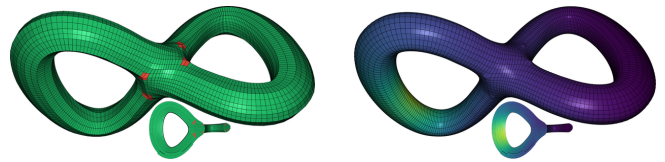


Fig. 12. Solution of the Poisson problem on a 3D hexahedral mesh.

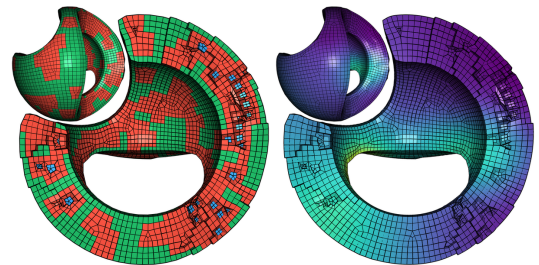


Fig. 13. Solution of the Poisson problem on a 3D hybrid mesh.



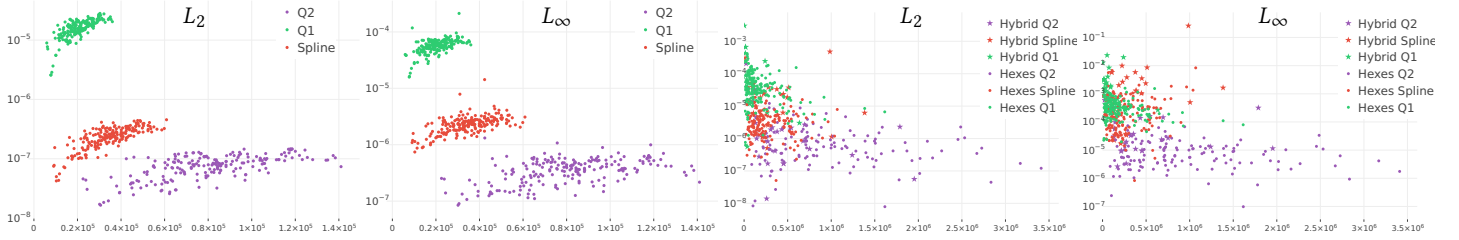


Fig. 14. Scatter plot of the  $L_2$  and  $L_\infty$  error versus the number of dofs on the 2D (first two) and 3D (last two) dataset.

**Memory.** A histogram of the memory consumption of the solver is presented in Figure 15. The figure shows the peak memory usage as reported by Pardiso [Petra et al. 2014b,a] when solving the linear system arising from the FEM. Out of the 159 pure hexahedral models we tested, 33 went out of memory when solving using  $Q_2$  elements, while only 2 are too big to solve with our spline bases. On the star-shaped hybrid meshes, one model is too big to solve for both  $Q_2$  and our spline construction. More detailed statistics are reported in Table 1.

**Convergence.** Figure 16 shows the convergence of spline elements vs  $Q_1$  and  $Q_2$  for the  $L_2$  and  $L_\infty$  norms, in the ideal case of a uniform grid, both in 2D and 3D. This is in a sense the best-case scenario that can be expected for our spline construction: every element is regular and has a  $3^2$  or  $3^3$  neighborhood. In this situation, splines exhibit a superior convergence  $> 3.0$  under both  $L_2$  and  $L_\infty$  norms.

On a 2D test mesh with mixing polygons and splines (model shown in Figure 10 top), we achieved a convergence rate of 2.8 in  $L_\infty$ , and 3.1 in  $L_2$  (Figure 17, left). Figure 17 also displays the convergence we obtained on a very simple hybrid 3D mesh, starting from a cube marked as a polyhedron, to which we applied our polar refinement described in Section 6. On this particular mesh, the splines exhibited a  $L_\infty$  convergence similar to  $Q_2$ , albeit being producing an error that is somewhat larger.

**Consistency Constraints.** Figure 18 shows the effect of our consistency constraint on the convergence of a polygonal mesh under refinement (the one shown in Figure 10, top), with  $Q_2$  elements used on the quadrilateral part. Without imposing any constraint on the bases overlapping the polygon, one can hope at best a convergence of  $\sim 2.0$ , whereas pure  $Q_2$  elements should have a convergence rate of 3.0. With a constraint ensuring linear reproduction for the bases defined on polyhedra, the convergence rate is still only  $\sim 2.5$ .

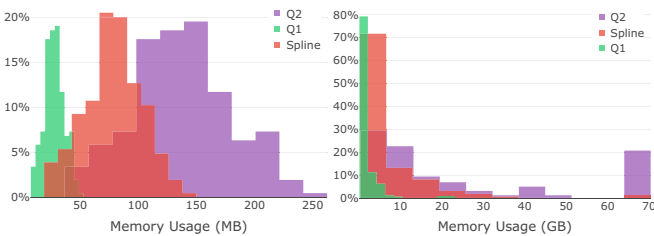


Fig. 15. Peak memory for the direct solver as reported by Pardiso. Left: 2D results. right: 3D results.

Finally, with the constraints we describe in Section 4.3 to ensure the bases reproduce triquadratic polynomials, we reach the expected convergence rate of  $\sim 3.0$ .

**Polyhedral Basis Resilience.** Our polyhedral bases are less susceptible to badly shaped elements than  $Q_2$ . We computed the  $L_2$  and  $L_\infty$  interpolation errors for the gradients of the Franke function for 14 badly shaped hexahedra, Figure 19 shows some of them. The  $L_2$  and  $L_\infty$  maximum and average errors are 3 times smaller with our polyhedral basis.

**Elasticity.** While most of our testing was done for the Poisson equation, we have performed some preliminary testing of linear elasticity problems. Figure 20 shows the solution of a linear elasticity problem on a pure hexahedral mesh. The outer loops of the knots are pulled outside of the figure, deforming the knot. The color in the figure represents the magnitude of the displacement vectors.

## 8 LIMITATIONS AND CONCLUDING REMARKS

We introduced Poly-Spline FEM, an integrated meshing and finite element method designed to take advantage of recent developments in hexahedral-dominant meshing, opening the doors to black box analysis with an high-order basis and cubic convergence under refinement. Our approach is to use the best possible basis for each element of the mesh and is amenable to continuous improvement, as the mesh generation methods and basis constructions improve.

		Num dofs	Solver Time	Memory (MiB)	$L_2$ Error	$L_\infty$ Error
$Q_1$	mean	193,243	1 min 41 s	1,391	$7.47 \times 10^{-5}$	$8.69 \times 10^{-4}$
	stdev	226,044	5 min 24 s	2,578	$2.34 \times 10^{-4}$	$2.50 \times 10^{-3}$
	min	3,201	0 min 0 s	5	$5.59 \times 10^{-7}$	$1.98 \times 10^{-5}$
	median	108,779	0 min 16 s	517	$3.16 \times 10^{-5}$	$3.27 \times 10^{-4}$
	max	1,614,258	49 min 27 s	21,365	$3.01 \times 10^{-3}$	$2.34 \times 10^{-2}$
$Q_2^*$	mean	878,228	32 min 45 s	11,697	$2.99 \times 10^{-6}$	$2.72 \times 10^{-5}$
	stdev	698,473	54 min 53 s	11,977	$1.68 \times 10^{-5}$	$7.08 \times 10^{-5}$
	min	22,805	0 min 3 s	100	$7.87 \times 10^{-9}$	$9.81 \times 10^{-8}$
	median	710,298	12 min 14 s	8,164	$6.02 \times 10^{-7}$	$9.14 \times 10^{-6}$
	max	3,409,814	300 min 12 s	50,617	$2.04 \times 10^{-4}$	$5.94 \times 10^{-4}$
Spline*	mean	286,460	12 min 54 s	5,363	$1.09 \times 10^{-5}$	$2.12 \times 10^{-3}$
	stdev	237,069	26 min 24 s	6,475	$4.20 \times 10^{-5}$	$1.92 \times 10^{-2}$
	min	11,267	0 min 2 s	68	$5.06 \times 10^{-8}$	$8.30 \times 10^{-7}$
	median	209,322	2 min 49 s	2,646	$3.40 \times 10^{-6}$	$2.08 \times 10^{-4}$
	max	1,383,354	215 min 3 s	35,315	$4.78 \times 10^{-4}$	$2.61 \times 10^{-1}$

Table 1. Dataset 3D pure hexahedra + star-shaped polyhedra (188 models in total). The memory is the total peak memory (in MiB) as reported by the solver Pardiso. \* does not include the models that went out of memory.

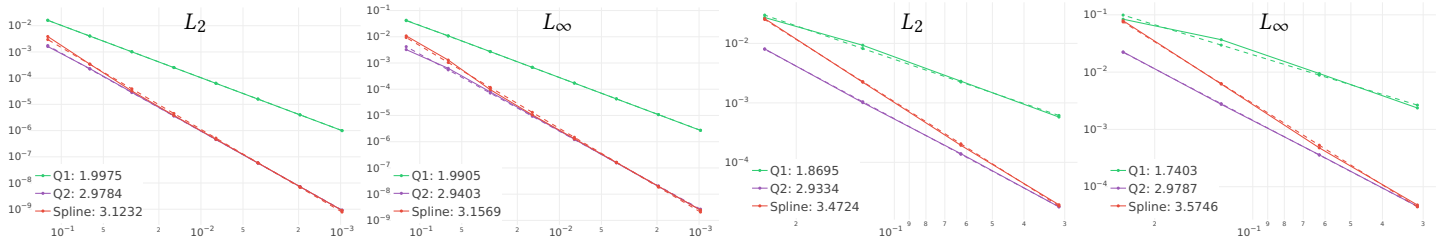


Fig. 16. Convergence plot in  $L_2$  and  $L_\infty$  norm on a regular grid in 2D (first two) and 3D (last two). The horizontal axis corresponds to the max edge length.

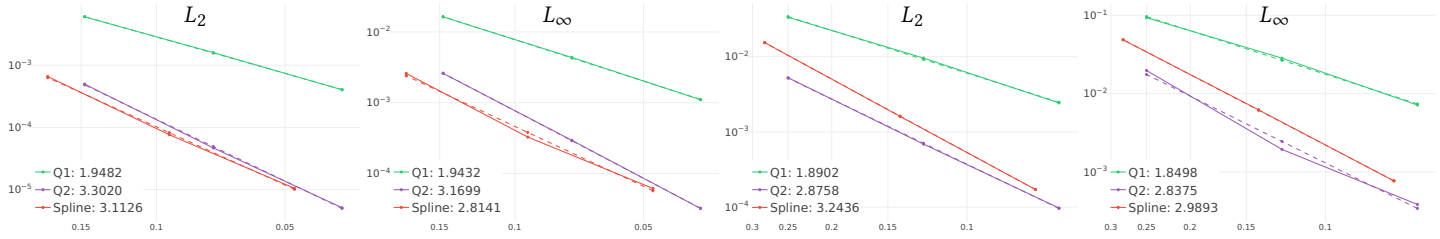


Fig. 17. Convergence plot in  $L_2$  and  $L_\infty$  norm for a hybrid mesh in 2D (first two) and 3D (last two). Meshes are show in Figure 10. The horizontal axis corresponds to the max edge length of  $g(\widehat{M})$ .

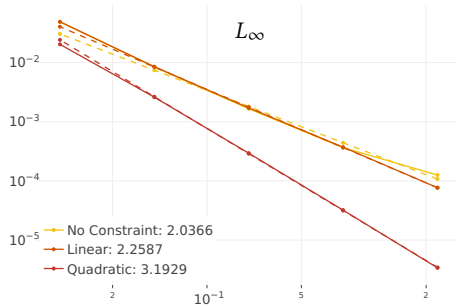


Fig. 18.  $L_\infty$  convergence for the different consistency constraints on a polyhedron.

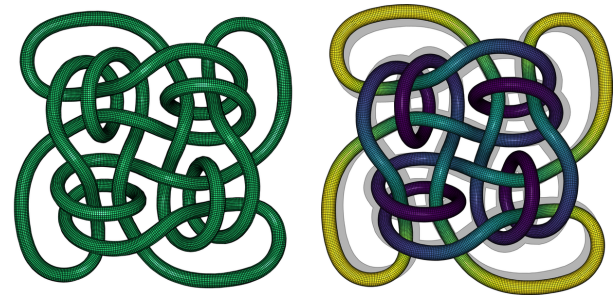


Fig. 20. Displacements computed solving linear elasticity on a pure hexahedral 3D model, using spline bases.

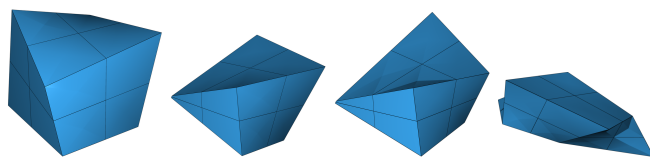


Fig. 19. Polygons used to measure the interpolation errors.

E.g., in this setting, one can avoid costly manual mesh repair and improvement, at the expense of modest increases in solution time, by switching to more expensive, but much less shape-sensitive elements when a hexahedron is badly shaped.

While our basis construction is resilient to bad element quality, the geometric map between the splines and the  $Q_2$  elements might introduce distortion (and even inversions in pathological cases), lowering convergence rate. These effects could be ameliorated by optimizing the positions of the control points of the geometric map, which is an interesting avenue for future work.

Our current construction relies on an initial refinement step to avoid polyhedra adjacent to other polyhedra or to the boundary. This limitation could be lifted by generalizing our basis construction, and would allow our method to process very large datasets unrefinable due to memory considerations. The constraints in our basis construction (Section 4.3) are PDE-dependent, and they thus require additional efforts to be used with a user-provided PDE: a small and reusable investment compared to the cost of manually meshing with hexahedra every surface that one wishes to analyze using  $Q_2$  elements.

Poly-Spline FEM is a practical construction in-between unstructured  $Q_2$  and fully-structured pure splines: it offers a smaller number of dofs than  $Q_2$  (thanks to the spline elements) while preserving cubic convergence. We believe that our construction will stimulate additional research in the development of heterogeneous FEM methods that exploit the regularity of spline basis and combine it with the flexibility offered by traditional FEM elements. To allow other researchers and practitioners to immediately build upon our

construction, we will release our entire software framework as an open-source project.

## A TEST FUNCTIONS

In our experiments, we use the test functions proposed in [Franke 1979]. For 2D:

$$f_{2D}(x_1, x_2) = \frac{3}{4}e^{-\frac{(9x_1-2)^2+(9x_2-2)^2}{4}} + \frac{3}{4}e^{-\frac{(9x_1+1)^2}{49}-\frac{9x_2+1}{10}} + \frac{1}{2}e^{-\frac{(9x_1-7)^2+(9x_2-3)^2}{4}} - \frac{1}{5}e^{-(9x_1-4)^2-(9x_2-7)^2},$$

and 3D:

$$f_{3D}(x_1, x_2, x_3) = \frac{3}{4}e^{-\frac{(9x_1-2)^2+(9x_2-2)^2+(9x_3-2)^2}{4}} + \frac{3}{4}e^{-\frac{(9x_1+1)^2}{49}-\frac{9x_2+1}{10}-\frac{9x_3+1}{10}} + \frac{1}{2}e^{-\frac{(9x_1-7)^2+(9x_2-3)^2+(9x_3-5)^2}{4}} - \frac{1}{5}e^{-(9x_1-4)^2-(9x_2-7)^2-(9x_3-5)^2}.$$

## REFERENCES

- M. Aigner, C. Heinrich, B. Jüttler, E. Pilgerstorfer, B. Simeon, and Vuong. 2009. *Swept volume parameterization for isogeometric analysis*. Springer.
- D. Arnold, D. Boffi, and R. Falk. 2002. Approximation by quadrilateral finite elements. *Mathematics of computation* 71, 239 (2002), 909–922.
- Y. Bazilevs, L. Beirão da Veiga, J. A. Cottrell, T. J. Hughes, and G. Sangalli. 2006. Isogeometric analysis: approximation, stability and error estimates for h-refined meshes. *Mathematical Models and Methods in Applied Sciences* 16, 07 (2006), 1031–1090.
- L. Beirão Da Veiga, F. Brezzi, A. Cangiani, G. Manzini, L. D. Marini, and A. Russo. 2013. Basic Principles Of Virtual Element Methods. *Mathematical Models and Methods in Applied Sciences* 23, 01 (2013), 199–214.
- S. E. Benzley, E. Perry, K. Merkley, B. Clark, and G. Sjaardema. 1995. A comparison of all hexagonal and all tetrahedral finite element meshes for elastic and elasto-plastic analysis. In *Proceedings of the 4th International Meshing Roundtable*. 179–191.
- J. Bishop. 2014. A displacement-based finite element formulation for general polyhedra using harmonic shape functions. *Internat. J. Numer. Methods Engng.* 97, 1 (2014), 1–31.
- D. Braess. 2007. *Finite elements: Theory, fast solvers, and applications in solid mechanics*. Cambridge University Press.
- A. O. Cifuentes and A. Kalbag. 1992. A performance study of tetrahedral and hexahedral elements in 3-D finite element structural analysis. *Finite Elements in Analysis and Design* 12, 3–4 (1992), 313–318.
- J. A. Cottrell, T. J. R. Hughes, and Y. Bazilevs. 2009. *Isogeometric Analysis: Toward Integration of CAD and FEA* (1st ed.). Wiley Publishing.
- L. B. da Veiga, A. Buffa, D. Cho, and G. Sangalli. 2011. IsoGeometric analysis using T-splines on two-patch geometries. *Comput. Meth. Appl. Mech. Eng.* 200, 21 (2011), 1787 – 1803. <http://www.sciencedirect.com/science/article/pii/S0045782511000405>
- B. A. de Dios, K. Lipnikov, and G. Manzini. 2016. The nonconforming virtual element method. *ESAIM: Mathematical Modelling and Numerical Analysis* 50, 3 (2016), 879–904.
- X. Fang, W. Xu, H. Bao, and J. Huang. 2016. All-hex meshing using closed-form induced polycube. *ACM Transactions on Graphics (TOG)* 35, 4 (2016), 124.
- M. S. Floater, G. Kós, and M. Reimers. 2005. Mean Value Coordinates in 3D. *Comput. Aided Geom. Des.* 22, 7 (Oct. 2005), 623–631.
- R. Franke. 1979. A Critical Comparison of Some Methods for Interpolation of Scattered Data. (1979). <https://calhoun.nps.edu/handle/10945/35052>
- X. Fu, C. Bai, and Y. Liu. 2016. Efficient Volumetric PolyCube-Map Construction. *Computer Graphics Forum (Pacific Graphics)* 35, 7 (2016).
- X. Gao, W. Jakob, M. Tarini, and D. Panozzo. 2017a. Robust Hex-dominant Mesh Generation Using Field-guided Polyhedral Agglomeration. *ACM Transactions on Graphics* 36, 4 (2017), 114:1–114:13.
- X. Gao, D. Panozzo, W. Wang, Z. Deng, and G. Chen. 2017b. Robust Structure Simplification for Hex Re-meshing. *ACM Trans. Graph.* 36, 6, Article 185 (Nov. 2017), 13 pages. DOI: <https://doi.org/10.1145/3130800.3130848>
- J. Gregson, A. Sheffer, and E. Zhang. 2011. All-Hex Mesh Generation via Volumetric PolyCube Deformation. *cgf* 30, 5 (2011), 1407–1416.
- K. Hormann and N. Sukumar. 2008. Maximum Entropy Coordinates for Arbitrary Polytopes. *Comput. Graph. Forum* 27, 5 (July 2008), 1513–1520. Proceedings of SGP.
- J. Huang, T. Jiang, Z. Shi, Y. Tong, H. Bao, and M. Desbrun. 2014. L1-based Construction of Polycube Maps from Complex Shapes. *ACM Trans. Graph.* 33, 3 (2014), 25:1–25:11.
- J. Huang, Y. Tong, H. Wei, and H. Bao. 2011. Boundary aligned smooth 3D cross-frame field. *ACM Trans. Graph.* 30, 6 (Dec. 2011), 143:1–143:8.
- T. J. Hughes, J. A. Cottrell, and Y. Bazilevs. 2005. Isogeometric analysis: CAD, finite elements, NURBS, exact geometry and mesh refinement. *Comput. Meth. Appl. Mech. Eng.* 194, 39 (2005), 4135–4195.
- T. J. R. Hughes. 2000. *The Finite Element Method. Linear Static and Dynamic Finite Element Analysis*. Dover Publications.
- Y. Ito, A. M. Shih, and B. K. Soni. 2009. Octree-based reasonable-quality hexahedral mesh generation using a new set of refinement templates. *Int. J. Numer. Meth. Engng* 77 (2009), 1809–1833.
- T. Jiang, J. Huang, Y. T. Yuanzhen Wang, and H. Bao. 2014. Frame Field Singularity Correction for Automatic Hexahedralization. *IEEE TVCG* 20, 8 (Aug. 2014), 1189–1199.
- P. Joshi, M. Meyer, T. DeRose, B. Green, and T. Sanocki. 2007. Harmonic Coordinates for Character Articulation. *ACM Transactions on Graphics* 26, 3 (July 2007), Article 71, 9 pages. Proceedings of SIGGRAPH.
- T. Ju, S. Schaefer, and J. Warren. 2005. Mean Value Coordinates for Closed Triangular Meshes. *ACM Transactions on Graphics* 24, 3 (July 2005), 561–566. Proceedings of SIGGRAPH.
- B. Li, X. Li, K. Wang, and H. Qin. 2013a. Surface Mesh to Volumetric Spline Conversion with Generalized Poly-cubes. *IEEE TVCG* 19, 9 (2013), 1539–1551.
- B. Li, X. Li, K. Wang, and H. Qin. 2013b. Surface mesh to volumetric spline conversion with generalized polycubes. *IEEE Trans. Vis. Comput. Graph.* 19, 9 (2013), 1539–1551.
- Y. Li, Y. Liu, W. Xu, W. Wang, and B. Guo. 2012. All-hex meshing using singularity-restricted field. *ACM Trans. Graph.* 31, 6 (Nov. 2012), 177:1–177:11.
- K. Lipnikov, G. Manzini, and M. Shashkov. 2014. Mimetic finite difference method. *J. Comput. Phys.* 257, Part B (2014), 1163–1227. Physics-compatible numerical methods.
- M. Livesu, N. Vining, A. Sheffer, J. Gregson, and R. Scateni. 2013. PolyCut: monotone graph-cuts for PolyCube base-complex construction. *ACM Trans. Graph.* 32, 6 (2013), 171.
- G. Manzini, A. Russo, and N. Sukumar. 2014. New perspectives on polygonal and polyhedral finite element methods. *Math. Meth. Appl. Sci.* 24, 08 (2014), 1665–1699.
- L. Maréchal. 2009a. *Advances in Octree-Based All-Hexahedral Mesh Generation: Handling Sharp Features*. Springer Berlin Heidelberg, Berlin, Heidelberg, 65–84.
- L. Maréchal. 2009b. Advances in octree-based all-hexahedral mesh generation: handling sharp features. In *proceedings of the 18th International Meshing Roundtable*. Springer, 65–84.
- S. Martin. 2011. Flexible, unified and directable methods for simulating deformable objects. (2011).
- S. Martin, P. Kaufmann, M. Botsch, M. Wicke, and M. Gross. 2008. Polyhedral Finite Elements Using Harmonic Basis Functions. In *Proceedings of the Symposium on Geometry Processing (SGP '08)*. Eurographics Association, 1521–1529. <http://dl.acm.org/citation.cfm?id=1731309.1731340>
- T. Martin and E. Cohen. 2010. Volumetric parameterization of complex objects by respecting multiple materials. *Comput. Graph.* 34, 3 (2010), 187–197.
- M. Nieser, U. Reitebuch, and K. Polthier. 2011. CubeCover- Parameterization of 3D Volumes. *cgf* 30, 5 (2011), 1397–1406.
- S. J. Owen and S. Saigal. 2000. H-Morph: an indirect approach to advancing front hex meshing. *Int. J. Numer. Methods Eng.* 49, 1–2 (2000), 289–312. [http://dx.doi.org/10.1002/1097-0207\(20000910\)49:1/2<289::AID-NME934>3.0.CO;2-L](http://dx.doi.org/10.1002/1097-0207(20000910)49:1/2<289::AID-NME934>3.0.CO;2-L)
- C. G. Petra, O. Schenk, and M. Anitescu. 2014a. Real-time stochastic optimization of complex energy systems on high-performance computers. *IEEE Computing in Science & Engineering* 16, 5 (2014), 32–42.
- C. G. Petra, O. Schenk, M. Lubin, and K. Gärtner. 2014b. An augmented incomplete factorization approach for computing the Schur complement in stochastic optimization. *SIAM Journal on Scientific Computing* 36, 2 (2014), C139–C162.
- T. W. Sederberg, D. L. Cardon, G. T. Finnigan, N. S. North, J. Zheng, and T. Lyche. 2004. T-spline Simplification and Local Refinement. *ACM Trans. Graph.* 23, 3 (Aug. 2004), 276–283. <http://doi.acm.org/10.1145/1015706.1015715>
- J. F. Shephard and C. R. Johnson. 2008. Hexahedral Mesh Generation Constraints. *Eng. with Comput.* 24, 3 (June 2008), 195–213.
- J. R. Shewchuk. 1996. *Triangle: Engineering a 2D quality mesh generator and Delaunay triangulator*. Springer Berlin Heidelberg, 203–222.
- H. Si. 2015. TetGen, a Delaunay-Based Quality Tetrahedral Mesh Generator. *ACM Trans. Math. Software* 41, 2 (Feb. 2015), 11:1–11:36.
- D. Sokolov, N. Ray, L. Untereiner, and B. Lévy. 2016. Hexahedral-Dominant Meshing. *ACM Trans. Graph.* 35, 5 (June 2016), 157:1–157:23.
- M. L. Staten, S. J. Owen, and T. D. Blacker. 2005. *Unconstrained Paving & Plastering: A New Idea for All Hexahedral Mesh Generation*. Springer Berlin Heidelberg, 399–416.
- D. Toshniwal, H. Speleers, R. R. Hiemstra, and T. J. Hughes. 2017. Multi-degree smooth polar splines: A framework for geometric modeling and isogeometric analysis. *Computer Methods in Applied Mechanics and Engineering* 316 (2017), 1005 – 1061. DOI: <https://doi.org/10.1016/j.cma.2016.11.009> Special Issue on Isogeometric Analysis: Progress and Challenges.
- S. Yamakawa and K. Shimada. 2003. Fully-automated hex-dominant mesh generation with directionality control via packing rectangular solid cells. *Int. J. Numer. Methods Eng.* 57, 15 (2003), 2099–2129. <http://dx.doi.org/10.1002/nme.754>

Y. J. Zhang, X. Liang, and G. Xu. 2013. A robust 2-refinement algorithm in octree or rhombic dodecahedral tree based all-hexahedral mesh generation. *Comput. Meth. Appl. Mech. Eng.* 256 (2013), 88–100.